Available online at www.sciencedirect.com
ScienceDirect
Journal of Power Sources 179 (2008) 209–219
JOURNAL OF POWER SOURCES
www.elsevier.com/locate/jpowsour

A comparison of different approaches to modelling the PEMFC catalyst layer

D. Harvey [a,b,d], J.G. Pharoah [a,b,*], K. Karan [a,c]

[a] *Queen's-RMC Fuel Cell Research Centre, Kingston, ON, Canada*
[b] *Department of Mechanical Engineering, Queen's University, Kingston, ON, Canada*
[c] *Department of Chemical Engineering, Queen's University, Kingston, ON, Canada*
[d] *Ballard Power Systems, Burnaby, BC, Canada*

Received 15 October 2007; received in revised form 13 December 2007; accepted 13 December 2007
Available online 3 January 2008

Abstract

This paper compares three different approaches for describing the cathode catalyst layer of a PEMFC, using a three-dimensional CFD model. The three catalyst treatments include: a thin-film model, a discrete-catalyst volume model and an agglomerate model. It is shown that, within a single-phase approach using physically meaningful parameters, the commonly employed thin-film or discrete-volume descriptions of the catalyst layer do not show the significant mass transport limitations which occur at higher current densities; while this region is observed using a catalyst agglomerate approach. Further, an in-depth analysis of the current density distributions indicates that for a given electrode overpotential the thin-film model significantly over-predicts the current density, compared to the discrete and agglomerate approaches. The thin-film model also greatly exaggerates the variation in current density both along and across the channel. Finally, the agglomerate model predicts noticeable mass transport losses even at very low current densities despite the use of high stoichiometric ratios and thin-electrolyte films.

Keywords: PEMFC; Catalyst Agglomerate; CFD; Performance Modelling; Cathode; Mass transport

1. Introduction

Fuel cells, particularly the polymer electrolyte membrane type, have long been touted as an environmentally friendly solution for automotive, backup, and residential power needs. However, despite the "green" image, fuel cells have yet to be implemented on a full commercial scale—due in a large part to cost, reliability, and lack of the necessary fuelling infrastructure. The optimization of the PEMFC related to cost and performance has been a long and on-going activity, both in academia and industry. As part of this on-going optimization activity, computational models are increasingly being applied in the design of the catalyst, porous transport layer (PTL, also known as the GDL), and flow-field plate; especially within the product optimization and research prototyping stages. In particular, computational fluid dynamics (CFD)-based models are finding increased use due in part to their ability to provide detailed spatial resolution of process variables such as species concentration, pressure, temperature, electrical potentials, and current density within the individual components of the unit cell. These variables are highly and non-linearly coupled to each other in the governing conservation equations and accordingly, each field variable influences and is influenced by the electrochemical reactions occurring in the catalyst layer. Clearly, it can be expected that the results produced by CFD models will be affected by the extent to which the physico–electro-chemical processes in the catalyst layer are considered. More specifically, the results of such models will depend greatly on the extent to which gradients in species concentration, temperature, and electrical potentials are accounted for. The three most common catalyst layer models are—(i) the agglomerate model [1,2], (ii) the discrete-volume model [3–6], and (iii) the thin-film model [7–9].

Among the three approaches, the agglomerate model is considered the most theoretically detailed as it attempts to include effects due to the catalyst's physical structure. In this approach,

* Corresponding author at: Queen's-RMC Fuel Cell Research Centre, Kingston, ON, Canada.
E-mail address: pharoah@me.queensu.ca (J.G. Pharoah).

0378-7753/$ – see front matter © 2008 Elsevier B.V. All rights reserved.
doi:10.1016/j.jpowsour.2007.12.077

Nomenclature

a_{agg}	effective agglomerate surface area ($m^2\ m^{-3}$)
a_{Pt}	theoretical platinum loading ($m^2\ m^{-3}$)
a_{scale}	scaling factor for non-agglomerate models
C	local species concentration ($mol\ m^{-3}$)
D	diffusivity of dissolved oxygen in the electrolyte ($m^2\ s^{-1}$)
D_{ij}	binary diffusion coefficient ($m^2\ s^{-1}$)
E_d	Activation energy for diffusion ($J\ mol^{-1}$)
E_{th}	Nernst voltage (V)
E_r	reaction effectiveness factor
H	Henry's constant ($Pa\ m^3\ mol^{-1}$)
i	current density ($A\ m^{-3}$)
i_o	local exchange current density ($A\ m^{-2}$)
k_c	reaction rate constant (s^{-1})
m_{Pt}	platinum loading ($kg\ m^{-2}$)
M_w	molecular weight ($kg\ mol^{-1}$)
NCO	nominal cathode overpotential (V)
r_{agg}	radius of the agglomerate particles (m)
r_{Pt}	platinum particle diameter (m)
S	volumetric source term
t	thickness (m)
u	x-component of the velocity vector ($m\ s^{-1}$)
v	y-component of the velocity vector ($m\ s^{-1}$)
V_k	atomic diffusion volume (m^3)
w	z-component of the velocity vector ($m\ s^{-1}$)
y	mass fraction
z	number of electrons consumed per mole of reactant ($mol(e^-)\ mol(reactant)^{-1}$)

Greek letters

α_c	cathodic transfer coefficient
δ	thickness of the electrolyte film covering the agglomerates (m)
ε_L	effective platinum surface ratio
η_{act}	activation overpotential (V)
μ	dynamic viscosity ($kg\ m^{-1}\ s^{-1}$)
ρ	density ($kg\ m^{-3}$)
σ_e	electronic conductivity ($S\ m^{-1}$)
ϕ	porosity and potential (V)
ϕ_{agg}	volume fraction of the electrolyte phase
ϕ_{RH}	relative humidity
Φ_L	Theile's modulus

Subscripts and superscripts

agg	agglomerate
cat	catalyst layer region
e	electronic or electrode
i	species i
op	operation point
p	protonic
PTL	porous transport layer region
rxn	reaction
sat	saturation point
th	theoretical value

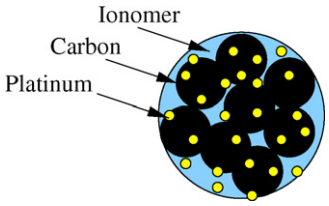

Fig. 1. A typical catalyst agglomerate.

the catalyst layer is considered to be comprised of numerous agglomerates, each of which is comprised of a cluster of carbon black particles with platinum catalyst dispersed on its surface. The Pt/C catalyst particles are held together by a polymeric electrolyte material, such as Nafion™. The catalyst agglomerates are generally considered to be of one of the following shapes—spherical, cylindrical or slab; with the pore space of the catalyst assumed to exist among the percolating network of agglomerates thereby allowing for fluid transport. The physical transport processes described by the agglomerate model include the gas-phase transport in the pore space of the catalyst layer, dissolution of chemical reactant in the electrolyte phase, simultaneous diffusion and reaction of the dissolved reactant within the agglomerate, ion transport in the electrolyte phase, and electron conduction via the carbon black particles. A representation of a single spherical agglomerate can seen in Fig. 1.

The physical description of the catalyst layer in the discrete-volume model is very similar to that of the agglomerate model with a few exceptions. The discrete-volume model does not consider the formation of agglomerates or any structure beyond the application of effective medium theory. As a result there is no consideration of the dissolution of reactants at the gas/Nafion™ interface, nor the simultaneous diffusion and reaction within the agglomerate structure itself. In one published variation of the discrete-volume model [10], the pore space of the catalyst is considered to be completely filled with water.

The thin-film model is very different from the discrete or agglomerate models; in this approach, the catalyst layer is not explicity described but is treated as a boundary condition at interface of the PTL and the membrane. The treatment of the catalyst layer as an interface means that it does not account for any transport or resistance in the physical structure of the catalyst layer.

In this paper, a half-cell PEMFC cathode model, developed in our research group, is applied to compare the predictions made using the three different catalyst layer models. The basis of comparison among the different models is made in terms of their predicted polarizations and spatial distribution of current densities. The results are interpreted in the context of two key factors affecting the current density and its distribution—oxygen concentration and overpotential.

2. Computational domain

The fuel cell considered in this paper represents a single channel of a parallel flow field, and as such, the model domain is greatly simplified compared to a serpentine flow-field in which convection in the PTL [11] must be considered due to the in-plane pressure gradients [12–14]. A typical computational

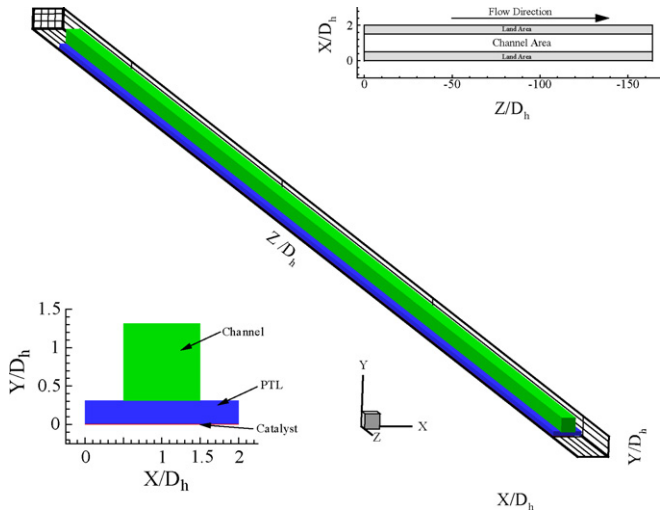

Fig. 2. Three-dimensional domain of a cathode with straight channels.

Table 1
Fuel cell geometry

Parameter	Value	Unit
Channel length, L	80	mm
Channel width, w_{ch}	1	mm
Channel height, h_{ch}	1	mm
Channel hydraulic diameter, D_h	1	mm
Land width, w_l	1	mm
PTL thickness, t_{PTL}	300	μm
PTL porosity, ϕ_{PTL}	0.4	
Catalyst thickness, t_{cat}	12.9	μm
Catalyst porosity, ϕ_{cat}	0.1	

domain used in this work is shown in Fig. 2; the length of the cell used in this study was 80 mm with a small inlet and outlet added upstream and downstream of the active area to port the gases to the flow channel. The domain represents the cathode flow-field, a PTL, and a catalyst layer. The computational domain was reduced to only one-half a landing and one-half a channel, as is shown in the cross-section of Fig 3, since the geometry and boundary conditions are symmetric about the line $x/D_h = 0$ (this is reasonable if convective effects – which can occur in straight channels due to poor plate manifolding – are neglected). Details of the geometry are given in Table 1, with the exception of the catalyst layer thickness for the thin-film model which is zero—consistent with the assumptions of the approach.

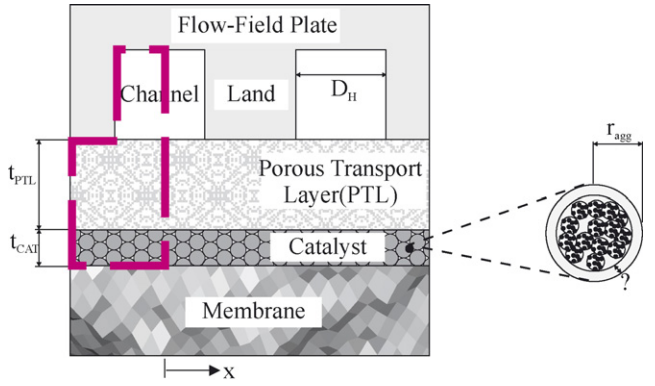

Fig. 3. Cross-section of the computational domain.

3. Transport phenomena

The cathode model is single phase, non-isothermal and accounts for electron/reactant transport in the PTL and proton/electron/reactant transport in the catalyst layer. The transport equations are solved using the commercial CFD solver Fluent 6.1 with the different catalyst models implemented through the use of custom-written user defined functions that effectively add source and sink terms within the catalyst layer, enforce specific boundary conditions, and implement specific material properties. Although the model is non-isothermal in that it accounts for heat generation due to, both, reaction and activations losses it was run isothermally for this investigation. It is important to emphasize that the accuracy of thermal boundary conditions, in particular the plate/coolant channels, and the material properties of both the MEA and plate are critical in achieving the correct temperature distribution through the MEA and are, for the moment, outside the scope of this work. All transport properties within the porous media are assumed to be isotropic, and the Bruggeman relation is used to estimate the effective mass diffusivities in the porous electrodes. Further details of the model are given in Ref. [13].

3.1. Gas flow channels

The flow within the gas supply channels was modelled as an ideal gas flow with the following governing equations.

3.1.1. Conservation of mass

$$\frac{\partial}{\partial x}(\rho u) + \frac{\partial}{\partial y}(\rho v) + \frac{\partial}{\partial z}(\rho w) = 0 \tag{1}$$

where ρ is the mixture density.

The density of the fluid mixture is determined using an ideal-gas mixing law:

$$\rho_{\text{mixture}} = \frac{P_{\text{op}}}{RT\sum_i (y_i/M_{\text{w},i})} \tag{2}$$

where P_{op} is the operating pressure, $M_{\text{w},i}$ is the molecular weight of species i, T is the temperature, R is the universal gas constant, and y_i is the mass fraction of species i.

3.1.2. Conservation of momentum

$$u\frac{\partial(\rho u)}{\partial x} + v\frac{\partial(\rho u)}{\partial y} + w\frac{\partial(\rho u)}{\partial z} = -\frac{\partial p}{\partial x} + \mu\nabla^2 u + S_{\text{mom}_x} \tag{3}$$

$$u\frac{\partial(\rho v)}{\partial x} + v\frac{\partial(\rho v)}{\partial y} + w\frac{\partial(\rho v)}{\partial z} = -\frac{\partial p}{\partial y} + \mu\nabla^2 v + S_{\text{mom}_y} \tag{4}$$

$$u\frac{\partial(\rho w)}{\partial x} + v\frac{\partial(\rho w)}{\partial y} + w\frac{\partial(\rho w)}{\partial z} = -\frac{\partial p}{\partial z} + \mu\nabla^2 w + S_{\text{mom}_z} \tag{5}$$

where S_{mom_x}, S_{mom_y}, and S_{mom_z} are momentum source terms for the x, y, z momentum equations, respectively. μ is the dynamic viscosity of the fluid mixture and is determined using a semi-

empirical formula [15]:

$$\mu = \sum_{i=1}^{n} \frac{x_i \mu_i}{\sum_{j=1}^{n} x_i \phi_{ij}} \tag{6}$$

with ϕ_{ij} determined by

$$\phi_{ij} = \frac{[1 + ((\mu_i/\mu_j))^{1/2}((M_{w,j}/M_{w,i}))^{1/4}]^2}{[8(1 + (M_{w,i}/M_{w,j}))]^{1/2}} \tag{7}$$

and the mole fraction, x_i, as

$$x_i = \frac{y_i/M_{w,i}}{\sum_{j=1}^{n}(y_i/M_{w,j})} \tag{8}$$

3.1.3. Species transport

For the purposes of this model, the dilute approximation for species transport was not considered; rather, a full multicomponent treatment of species diffusion was used. The general form of the equation describing the species transport is [16]:

$$\nabla \cdot (\rho \vec{v} y_i) = -\nabla \cdot \vec{\mathbf{J}}_i \tag{9}$$

where $\vec{\mathbf{J}}_i$ is the diffusive mass flux vector for species i and was described by the Maxwell–Stefan equation for multicomponent mixtures:

$$\vec{\mathbf{J}}_i = -\sum_{j=1}^{N-1} \rho D_{ij} \nabla y_j \tag{10}$$

The Maxwell–Stefan diffusion coefficients can be approximated with the binary coefficients [17] and were determined using the Fuller, Shettler, and Giddings empirical correlation [18]:

$$D_{ij} = \frac{T^{1.75}((1/M_{w,i}) + (1/M_{w,j}))^{1/2}}{p((\Sigma_k V_{k,i})^{1/3} + (\Sigma_k V_{k,j})^{1/3})} \times 10^{-8} \tag{11}$$

where $V_{k,i}$ and $V_{k,j}$ are the atomic mass volumes for species i and j, respectively; these values are tabulated in Cussler [18] for several common compounds.

3.2. Porous transport layer

The PTL is a porous media and as a result, the governing equations presented for the flow channel still apply; but, with modifications that account for the porous effects.

3.2.1. Conservation of mass

$$\nabla \cdot (\rho v_{Darcy}) = 0 \tag{12}$$

where v_{Darcy} is the Darcy or superficial velocity and is based on the volumetric flow rate of the porous media [16]. The superficial velocity is related to the physical or intrinsic velocity of the porous media by the Dupuit–Forcheimer relationship [19]:

$$v_{Darcy} = \phi_{PTL} v_{physical} \tag{13}$$

where $v_{physical}$ is the local volume average of the fluid velocity.

In the present model, the superficial velocity was used; however, the mass flow rate entering the porous media is determined using the superficial velocity and as such the total pressure drop across the media was the same for both formulations [16].

3.2.2. Conservation of momentum

The porous media in this study was modelled through the inclusion of a momentum source term within the general momentum equations; this source term consisted of two subterms—a viscous loss and an inertial loss:

$$S_{mom_i} = -\left(\sum_{j=1}^{3} D_{ij} \mu v_j + \sum_{j=1}^{3} C_{ij} \frac{1}{2} \rho v_{mag} v_j\right) \tag{14}$$

where C and D are diagonal matrices that contain the inertial resistance factor and inverse of the permeability, respectively.

A Darcy flow regime is assumed for flow in the porous media, such that the non-linear term is negligible and Eq. (14) reduces to

$$S_{mom_i} = -\left(\frac{\mu}{k} v_i\right) \tag{15}$$

where k is the permeability of the porous media.

3.2.3. Species transport

The species transport equation in the porous media was as follows, with a modification to account for the porosity [19]:

$$\nabla \cdot (\rho \vec{v} y_i) = -\nabla \cdot (\phi_{PTL} \vec{\mathbf{J}}_i) \tag{16}$$

where $\vec{v}$ is the superficial velocity (recalling the relationship with the physical velocity in Eq. (13)). The diffusive flux vector, $\vec{\mathbf{J}}_i$, is corrected using an effective binary diffusivity value which reflects the existence of the porous media:

$$\vec{\mathbf{J}}_i = -\sum_{j=1}^{N-1} \rho D_{eff} \nabla y_j \tag{17}$$

where D_{eff} is determined by a Bruggemann-type correction [20]:

$$D_{eff} = D_{ij} \phi_{PTL}^{1.5} \tag{18}$$

3.2.4. Conservation of charge

The transport of electrons through the solid phase of the porous medium was described using Ohm's law [21]:

$$-\nabla \cdot (\sigma_e \nabla \phi_e) = 0 \tag{19}$$

where σ_e is the specific electronic conductivity of the solid material in the PTL and ϕ_e is the electronic potential.

3.3. Catalyst layer

The catalyst layer was modelled as a porous media, similar to the PTL; therefore, the equations governing the physics of the PTL are the same as those within the catalyst with the exception that the catalyst region includes an extra equation that governs the transport of protons and an appropriate set of

sources and sinks that account for the processes of generation and consumption based on the cathode half-cell reaction.

3.3.1. Conservation of mass

$$\nabla \cdot (\rho v) = S_{\text{mass}} \tag{20}$$

where S_{mass} is a source of mass per unit volume:

$$S_{\text{mass}} = S_{\text{H}_2\text{O}} + S_{\text{O}_2} \tag{21}$$

with $S_{\text{H}_2\text{O}}$ and S_{O_2} as the source terms for water and oxygen per unit volume, respectively.

3.3.2. Conservation of momentum

Recalling the Darcy-like form of Eq. (15), the momentum equations for the catalyst layer are

$$\nabla \cdot (\rho \vec{v}\vec{v}) = -\nabla p + \mu \nabla^2 v - \frac{\mu}{k}\vec{v} + S_{\text{mom}_{\text{rxn}}} \tag{22}$$

where $S_{\text{mom}_{\text{rxn}}}$ is the source term for the ith momentum equation in x, y, z which is included to account for the effect of the added mass resulting from the electrochemical reaction:

$$S_{\text{mom}_{\text{rxn}}} = S_{\text{mass}} v_i \tag{23}$$

3.3.3. Species transport

The transport of species is governed by the following, with the addition of a source term to account for the consumption/generation of reactants/products by the electrochemical reaction:

$$\nabla \cdot (\rho \vec{v} y_i) = -\nabla \cdot (\phi_{\text{cat}} \vec{\mathbf{J}}_i) + S_i \tag{24}$$

where S_i is the source of species i per unit volume.

The source terms for each species were determined based on the cathode half-cell reaction with the following equation representing the amount of species i (oxygen or water) which was consumed/generated by the electrochemical reaction:

$$S_{i_{\text{rxn}}} = -\frac{M_{\text{w},i}}{z_i F} i \tag{25}$$

where z_i is the number of electrons consumed per mole generated/consumed of species i, F is Faraday's constant, and i is the local source of current per unit volume.

In addition to the water generated by the electrochemical reaction, there is also a movement of water between the anode and the cathode. Typically, this interchange of water is considered to be the result of three separate mechanisms—electro-osmotic drag due to the potential gradient in the charge carrier, back-diffusion resulting from a concentration gradient in water, and convection due to pressure gradients that arise from membrane swelling (capillary pressure and elastic stresses) [22–24]. The transport of water across the membrane due to the mechanism of convection is not considered and is referred for future work. Generally, the movement of water due to electro-osmotic drag is described through the use of a drag coefficient that describes the number of water molecules transported per charge carrier (H^+), this value ranges from 0.1 to 2.5 in the literature [25–28]. The back-diffusion of water from the cathode to the anode is expressed as a function of the local water concentration gradient. These two effects, electro-osmotic drag and back-diffusion, are generally combined into a single expression known as the net drag coefficient of water [24,25,27,29]. This net drag coefficient was measured by Choi et al. [30] and was then correlated with current density and cathode potential by Sun et al. [1]:

$$\alpha_{\text{H}_2\text{O}} = \begin{cases} 1.0, & \text{NCO} < 0.25\,\text{V} \\ 46 \times \text{NCO}^2 - 31.52 \times \text{NCO} + 5.7, & 0.25\,\text{V} \geq \text{NCO} \leq 0.35\,\text{V} \\ 0.3, & \text{NCO} > 0.35\,\text{V} \end{cases} \tag{26}$$

where NCO is the nominal cathode overpotential and is outlined in Eq. (37).

The overall contribution of the water flux across the membrane is described by

$$S_{\text{H}_2\text{O}_{\text{flux}}} = \frac{2\alpha M_{\text{H}_2\text{O}}}{z_{\text{H}_2\text{O}} F} i \tag{27}$$

The total source of water is then

$$S_{\text{H}_2\text{O}} = S_{\text{H}_2\text{O}_{\text{rxn}}} + S_{\text{H}_2\text{O}_{\text{flux}}} \tag{28}$$

3.3.4. Conservation of charge

Electron transport. Electrons in the catalyst are transported through the solid phase (platinum and the graphite or carbon supporting matrix) by means of conduction:

$$-\nabla \cdot (\sigma_{\text{e}_{\text{cat}}} \nabla \phi_{\text{e}}) = S_{\text{e}} \tag{29}$$

where S_{e} is the local source of electric current per unit volume and within the catalyst layer the specific electronic conductivity is a function of the catalyst porosity and Nafion™ volume fraction in the agglomerate:

$$\sigma_{\text{e}_{\text{cat}}} = \sigma_{\text{e}}[(1 - \phi_{\text{cat}})(1 - \phi_{\text{agg}})]^{1.5} \tag{30}$$

Proton transport. Protons generated in the anode reaction are transported by the solid polymer membrane from the anode to the cathode and are transported in the catalyst layers via the Nafion™. This process can be described by

$$-\nabla \cdot (\sigma_{\text{p}} \nabla \phi_{\text{p}}) = S_{\text{p}} \tag{31}$$

where S_{p} is the local source of protonic current per unit volume, ϕ_{p} is the protonic phase potential, and σ_{p} is the specific protonic conductivity.

The conductivity of the Nafion™ phase that exists within the catalyst is dependent on the local water content and is assumed to follow the relationship reported by Springer et al. [31](this relationship will vary with different ionomers types):

$$\sigma_{\text{p}} = 100(5.139e^{-3}\lambda - 3.26e^{-3}) \exp\left[1268\left(\frac{1}{303} - \frac{1}{T_{\text{o}}}\right)\right] \tag{32}$$

where λ is the local water content of the Nafion™ and is a function of the local relative humidity. This equation is valid for relative humidities less than or equal to unity—above unity Schroeder's Paradox occurs (given the single-phase nature of

this work- –Shroeder's Paradox is currently neglected). The relationship between local humidity and membrane water content was described by Hinatsu et al. [32]:

$$\lambda = 0.3 + 10.8\phi_{RH} - 16\phi_{RH}^2 + 14.1\phi_{RH}^3 \quad (33)$$

where ϕ_{RH} is the relative humidity and was determined by

$$\phi_{RH} = \frac{P_{H_2O}}{P_{H_2O,sat}} \quad (34)$$

with P_{H_2O} as the local partial pressure of water and $P_{H_2O,sat}$ as the local saturation pressure of water—determined by a regression of the data in Ref. [33]:

$$P_{H_2O,sat} = 1.26837 \times 10^{-3}T^4 - 1.49827T^3 + 6.70916 \times 10^2 T^2 - 1.34832 \times 10^5 T + 1.02503 \times 10^7 \quad (35)$$

3.4. Activation overpotential and cathode potential

The activation overpotential is a measure of the voltage losses that result from driving the electrochemical reaction at the electrode [34]. Through consideration of the phase potentials, the activation overpotential can be evaluated via the following [1,35]:

$$\eta_{act} = \phi_{e,local} - \phi_{p,local} - \phi_{ref} \quad (36)$$

where $\phi_{e,local}$ is the local electronic potential, $\phi_{p,local}$ is the local protonic potential, and ϕ_{ref} is the desired reference electrode.

With respect to this model, the reference electrode has been chosen as the oxygen electrode (similar to that of Sun et al. [1,36]); as such the reference electrode potential is zero.

The cathode potential or nominal cathode potential (NCO) is the difference between the electronic phase potential at the collector plate (bi-polar plate) and the protonic phase potential at the catalyst/membrane interface. This term is a description of the total losses in the cathode—activation losses, ohmic losses due to electron transport in the catalyst and PTL, ohmic losses due to protonic transport in the catalyst, and mass-transport losses. It follows that the operating cathode voltage can be described by

$$V_{cathode} = E_{th} - NCO \quad (37)$$

where E_{th} is the Nernst voltage [34]:

$$E_{th} = E^o + \frac{RT}{2F} \ln\left(\frac{a_{H_{2g}} a_{O_{2g}}^{1/2}}{a_{H_2O_l}}\right) \quad (38)$$

where E^o is the open circuit voltage at the specific operating temperature and $a_{H_{2g}}$, $a_{O_{2g}}$, $a_{H_2O_l}$ are the activities of gaseous hydrogen, gaseous oxygen, and liquid water, respectively.

For the purposes of determining the open circuit voltage; the total pressure on the anode is assumed to be 1 atm and have a humidification level of 100%.

3.5. Approaches to catalyst layer modelling

The following section outlays the methodologies and equations for each catalyst modelling approach: agglomerate, discrete-volume, and thin-film interface.

3.5.1. Agglomerate catalyst model

In this approach the transport processes within the catalyst are assumed to be described by the following:

- Dissolution of oxygen across the gas–Nafion™ interface.
- Diffusion of dissolved oxygen within the Nafion™ electrolyte.
- Diffusion of dissolved oxygen within the agglomerate structure.

The agglomerate catalyst model is described by the standard Butler–Volmer kinetics [35]:

$$i = a_{Pt}^{eff} i_o \frac{C_{O_2}}{C_{O_2}^{ref}} \left[\exp\left(-\frac{\alpha_c F}{RT}\eta_{act}\right) - \exp\left(\frac{(1-\alpha_c)F}{RT}\eta_{act}\right)\right] \quad (39)$$

following a detailed re-arrangement, with consideration for the mechanisms of oxygen transport within the catalyst, the governing kinetics take the following form [1]:

$$i = zF\frac{P_{O_2}}{H}\left(\frac{1}{E_r k_c(1-\phi_{cat})} + \frac{(r_{agg}+\delta)\delta}{a_{agg} r_{agg} D}\right)^{-1} \quad (40)$$

where E_r is an effectiveness factor of the spherical agglomerate, z is the number of electrons involved in the reaction per mole of reactant, H is Henry's Constant, a_{agg} is the effective agglomerate surface area, r_{agg} is the agglomerate radius, δ is the thickness of the Nafion™ film, D is the diffusivity of the dissolved oxygen in Nafion™, and k_c is a reaction rate constant.

The effectiveness factor of the spherical agglomerate is also a measure of the effectiveness of the electrode reaction and can be found via:

$$E_r = \frac{1}{\Phi_L}\left(\frac{1}{\tanh(3\Phi_L)} - \frac{1}{3\Phi_L}\right) \quad (41)$$

with Φ_L, Theile's modulus for chemical reactions, as

$$\Phi_L = \frac{r_{agg}}{3}\sqrt{\frac{k_c}{D_{eff}}} \quad (42)$$

where D_{eff} is the effective diffusivity of dissolved oxygen in Nafion™ within the agglomerate structures and is determined using a Bruggemann-type correction:

$$D_{eff} = D\phi_{agg}^{1.5} \quad (43)$$

with ϕ_{agg} as the volume fraction of Nafion™ in the porous media and D as the diffusivity of dissolved oxygen in Nafion™ [37]:

$$D = 4.38 \times 10^{-6} \exp\left(-\frac{E_d}{RT}\right) \quad (44)$$

E_d is the activation energy for diffusion and was determined from the data presented by Parthasarathy et al. [37].

Henry's constant is determined using the relationship of [38]:

$$\frac{1}{H_2} = \frac{1}{H_1} \exp\left[-\frac{\Delta G_s}{R}\left(\frac{1}{T_2} - \frac{1}{T_1}\right)\right] \quad (45)$$

where ΔG_s is the free energy of dissolution and is approximately $-5209.69\ \mathrm{J\,mol^{-1}}$.

The reaction rate constant, k_c, is

$$k_c = \left(\frac{a_{Pt}^{eff}}{zF(1-\phi_{cat})1}\right)\left[\frac{i_o}{C_{O_2}^{ref}}\right]\left[\exp\left(-\frac{\alpha_c F}{RT}\eta_{act}\right) - \exp\left(\frac{(1-\alpha_c)F}{RT}\eta_{act}\right)\right] \quad (46)$$

where a_{Pt}^{ref} is the effective platinum surface area per unit catalyst layer volume, i_o is the exchange current density at temperature, T, $C_{O_2}^{ref}$ is the reference oxygen concentration, and η_{act} is the local activation overpotential.

The exchange current density, i_o, was calculated using the reference exchange current density, corrected for local temperature (this form was used in each catalyst model):

$$i_o = i_o^{ref} \exp\left[-\frac{E_{act}}{R}\left(\frac{1}{T} - \frac{1}{T_o}\right)\right] \quad (47)$$

where i_o^{ref} is the reference exchange current density at the reference temperature, T_o.

a_{Pt}^{ref} is a function of the specific surface area per unit catalyst volume, a_{Pt} and an effectiveness factor, ε_L, which accounts for the portions of the catalyst that are unable to meet the requirements for electrochemical reaction (i.e. electrically, protonically, and/or gas-phase isolated):

$$a_{Pt}^{ref} = \varepsilon_L a_{Pt} \quad (48)$$

a_{Pt} was determined from:

$$a_{Pt} = \frac{3m_{Pt}}{r_{Pt}\rho_{Pt}t_{cat}} \quad (49)$$

where m_{Pt}, ρ_{Pt}, and t_{cat} are the platinum loading, density of platinum, and catalyst layer thickness, respectively.

3.5.2. Discrete-catalyst model

Within this method, the catalyst is considered to be governed by the standard Butler–Volmer type kinetics, as in the agglomerate model, however this method gives no consideration for the transport of oxygen through the electrolyte phase. The model does consider the resistance posed by the layer for reactant and charged species transport.

The standard Butler–Volmer kinetics are

$$i = a_{scale} i_o \frac{C_{O_2}}{C_{O_2}^{ref}}\left[\exp\left(-\frac{\alpha_c F}{RT}\eta_{act}\right) - \exp\left(\frac{(1-\alpha_c)F}{RT}\eta_{act}\right)\right] \quad (50)$$

where a_{scale} is a scale factor used to adjust for the active area of the catalyst in order to calibrate the cathode polarization curves for each of the non-agglomerate approaches and C_{O_2} is the local gas concentration of oxygen; this is a major differing point with the agglomerate model which instead considers the concentration of dissolved oxygen.

Table 2
Operating conditions

Parameter	Value	Unit
Stoichiometric ratio, λ	5.0	
Inlet relative humidity, ϕ_{RH}	0.5	
Inlet temperature, T	50	°C
Operating pressure, P	1.5	atm

3.5.3. Thin-interface catalyst model

The thin-interface approach treats the catalyst in a manner that it is considered as only a layer of source terms for reactants, energy, and electrons [39]. This is achieved by considering the catalyst as having only a single control volume in the thickness direction and neglecting the heat transfer, proton transport, electron transport, reactant transport, and activation overpotential distributions that occur within the catalyst. This method is governed by the same form of the Butler–Volmer kinetics as shown in Eq. (50).

3.6. Operating conditions

The operating conditions employed in this work are given in Table 2 while the catalyst parameters are given in Table 3. The stoichiometric ratio was deliberately set high ($\lambda = 5.0$) in order to minimize the mass transport effects which occur due to reactant consumption. If significant differences between the approaches are noted under these conditions, they are certain to be of even more importance under realistic flow rates. Also of note is the fact that the inlet relative humidity was held at 50% in order to prevent the formation of liquid water in the PTL

Table 3
Catalyst and PTL properties

Parameter	Value	Unit	Reference
Platinum loading, m_{Pt}	4	$\mathrm{g\,m^{-2}}$	[13]
Platinum radius, r_{Pt}	1.5	nm	[1]
Agglomerate radius, r_{agg}	1	μm	[1]
Eff. agglomerate area, a_{agg}	3.6×10^5	$\mathrm{m^2\,m^{-3}}$	[1]
Ref. Exch. current density, i_o^{ref}			
$E_{cell} \geq 0.8$ V	3.85×10^{-4}	$\mathrm{A\,cm^{-2}}$	[38]
$E_{cell} < 0.8$ V	1.5×10^{-2}	$\mathrm{A\,cm^{-2}}$	
Activation energy, E_{act}			
$E_{cell} \geq 0.8$ V	76.5×10^3	$\mathrm{J\,mol^{-1}}$	[38]
$E_{cell} < 0.8$ V	27.7×10^3	$\mathrm{J\,mol^{-1}}$	
Charge transfer, α_c			
$E_{cell} \geq 0.8$ V	1.0		[38]
$E_{cell} < 0.8$ V	0.55		
Ref O_2concentration, $C_{O_2,ref}$	0.85	$\mathrm{mol\,m^{-3}}$	[38]
Henry's constant, H	0.2685×10^5	$\mathrm{Pa\,m^3\,mol^{-1}}$	[37]
Effective Pt surface ratio, ε_L	0.75		[41]
Electrolyte fraction, ϕ_{agg}	0.5		[42]
PTL conductivity, σ_{PTL}	100	$\mathrm{S\,m^{-1}}$	[13]

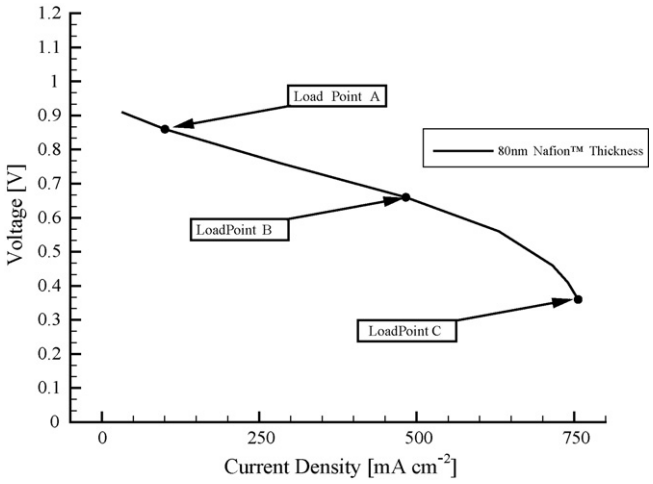

Fig. 4. Cathode polarization curve for the agglomerate model with $\delta = 80$ nm.

and channels, as the physics of liquid water transport are not included in this model. An inlet value of $\phi_{RH} = 50\%$ was found adequate to keep the relative humidity everywhere below 100%, and this is supported experimentally by recent neutron imaging data [40].

3.7. Boundary conditions

A fully developed laminar flow profile is assumed at the channel inlet with the properties given in Table 2. The electronic phase potential is set to zero on the landing surface and a zero flux of electrons is imposed on the membrane/catalyst interface. The ionic phase potential is set to the desired load point at the catalyst/membrane interface and a zero flux of protons is enforced at the catalyst/PTL boundary. All equations employ symmetry on the $x/D_h = -1$ surface and the $x/D_h = 0$surface. The outlet condition assumes a zero gradient in the flow direction for all variables, with the exception of pressure.

4. Results

4.1. Catalyst agglomerate model

The catalyst agglomerate model is the most detailed of the catalyst models described in this paper in that it accounts for more physical processes and a better description of the actual morphology of the catalyst layer. As such, it is considered – for the purposes of this paper – to be the baseline against which the other two models will be compared.

Fig. 4 shows the polarization curve predicted with the catalyst agglomerate model using a Nafion^{TM} film thickness of $\delta = 80$ nm and demonstrates that the model is capable of capturing all the relevant features of a typical polarization curve, including the sharp drop off in performance at high current. Three load points are identified on the figure, corresponding to each of the 'classic' regimes: (A) activation dominated losses at low current, (B) ohmic dominated losses at mid-range current and (C) mass transport dominated losses at high current.

Fig. 5 shows the predicted current density distribution normalized by the load point average current at a location very near the inlet. The results are in good agreement with the two-dimensional predictions of Sun et al. [1] and aid in understanding the limiting factor in current production for the chosen load points. At each point, the local reaction rate is dependant upon, both, the oxygen concentration at the reaction site, and the local overpotential; which is a function of the local ionic end electronic potentials.

At low currents (load point A) there is relatively little oxygen consumption, and as such the reaction rate is limited by the transport of electrons through the PTL which results in the maximum current production occurring under the land area where electrons are most accessible. As the current is increased (load point B); both, electron transport and oxygen transport become important such that the location of maximum current production shifts to the interface between the land and the channel. Finally, at high currents (load point C), the transport of oxygen limits the reaction, and the maximum current production is now occurring under the channel where the oxygen is most abundant.

A significant observation here is that the effect of the mass transport limitations are clearly evident in the case of load point B even though this load point is firmly located in the linear, or 'classic' ohmic, region of the polarization curve. In hindsight, this should not be an unexpected effect; polarizations curves are concave up at low current and concave down at high current and there must be an inflection point somewhere in between. This inflection point is the location where mass transport losses actually begin to become significant and is usually quite subtle as the dominating loss is transitioning from one mechanism to another.

We now turn our attention to the three-dimensional effects that occur along the channel. For both load points A and C (not shown), the current density distributions are very similar to those in Fig. 5 with a decreasing magnitude as the distance along the channel increases. However, this is not the case for load point B; Fig. 6 depicts the current density distribution for load point B at three locations along the channel. Near the inlet, the maximum current density is located near the land/channel

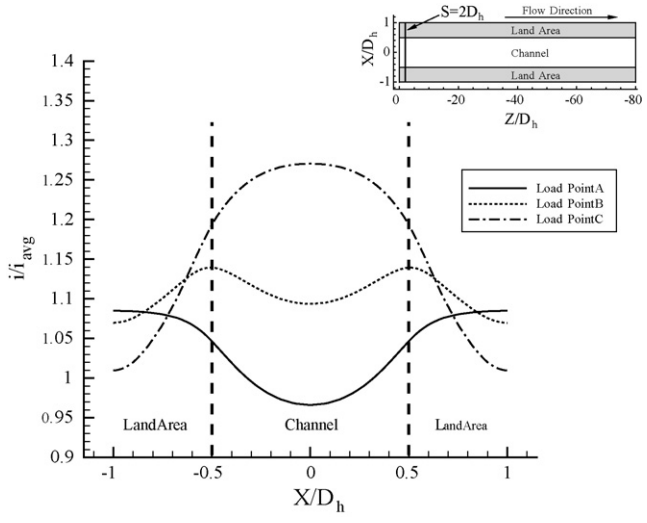

Fig. 5. Current density distribution near the inlet for three load points.

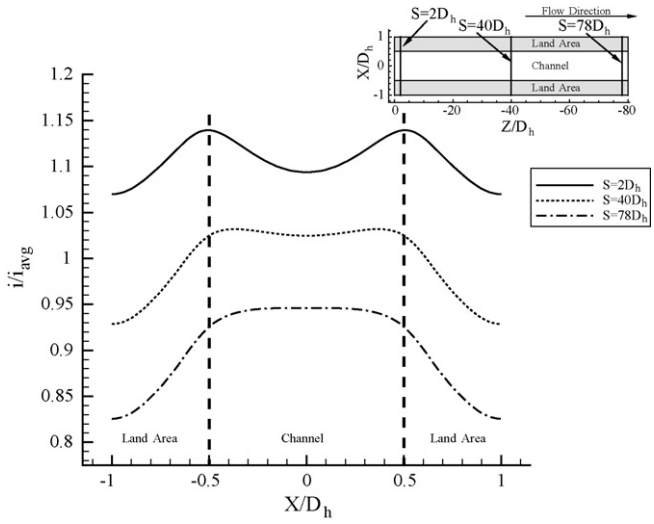

Fig. 6. Current density distribution at three locations along the channel for load point B.

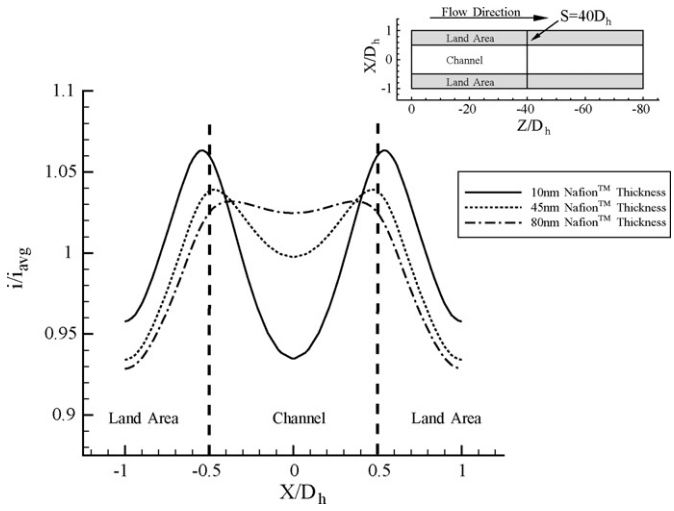

Fig. 8. Current density distribution at $z/D_h = 40$ for load point B.

interface. Moving down the channel, the location of the maximum clearly shifts towards the centre of the channel region, indicating the increasing importance of oxygen mass transport limitations even at moderate current densities.

The sole 'free' parameter in the catalyst agglomerate model is the thickness of the electrolyte film surrounding the catalyst agglomerates, δ. This value was estimated to be approximately 80 nm in the two-dimensional work of Sun et al. [1] in part because this number gave reasonable values for the predicted mass transport limited current densities. The initial three-dimensional work retained this thickness, and it was found that the predicted current density dropped sharply owing the oxygen depletion along the channel which is not accounted for in two dimensional models. Accordingly, this parameter was varied, and the resulting polarization curves are depicted in Fig. 7. As δ is decreased, the limiting current increases dramatically, such that a value closer to 35 nm is needed to predict overall current densities similar to the two-dimensional case of Sun et al.

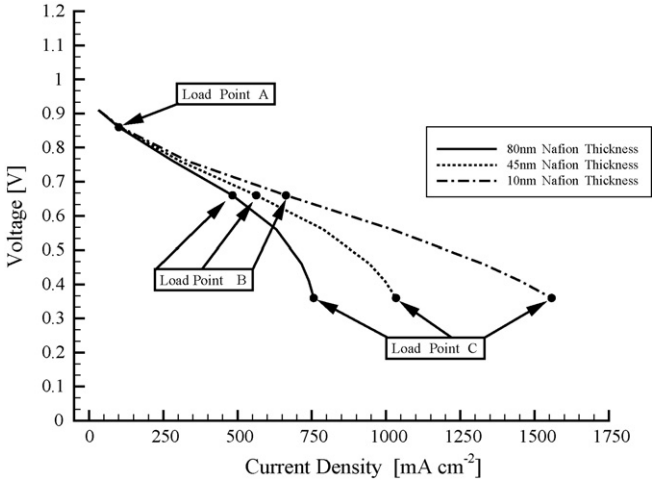

Fig. 7. Cathode polarization curve for varying Nafion™ thickness.

It is additionally interesting to note that changing the electrolyte thickness also changes the relative importance of mass transport losses compared to electron transport (ohmic) losses, as evidenced in Fig. 8. This figure compares the current distribution for load point B at the mid-point between the inlet and the outlet of the fuel cell. For the lowest electrolyte thickness, the location of the maximum current is at the land/channel interface, with a significant local minimum at the channel centreline. However, as δ increases the current distribution begins to flatten almost to the point where the maximum current production is located under the channel region. These results emphasize that there is clearly a significant need to experimentally characterize the electrolyte film thickness in catalyst layer; particularly, if accurate predictions of current gradients and overall electrode performance is desired.

4.2. Comparison of catalyst models

The vast majority of (CFD-based) fuel cell models do not yet use agglomerate type models, and as such represent simplifications with respect to the real catalyst morphology. The agglomerate model is itself a simplification compared to the true morphology of the catalyst, but yet less so compared to the commonly employed discrete-volume or thin-interface approaches. Significant mass transport losses occur due to dissolved oxygen transport in the electrolyte phase and these losses are accounted for in the agglomerate model. In the absence of a mechanism to account for these losses, conventional single-phase catalyst models are unable to capture the sharp drop off in the polarization curve observed at high currents. For this reason, it was decided to compare the results of the agglomerate model to the discrete catalyst and thin-interface catalyst model using a low film thickness of 10 nm. This tends to minimize the differences between the models, and as such, the identified differences will be more significant with realistic thicknesses.

Fig. 9 shows the predicted polarization curve using each of the three models. In the case of the discrete and thin-interface models; the parameter, a_{scale}, in the Butler–Volmer equation was

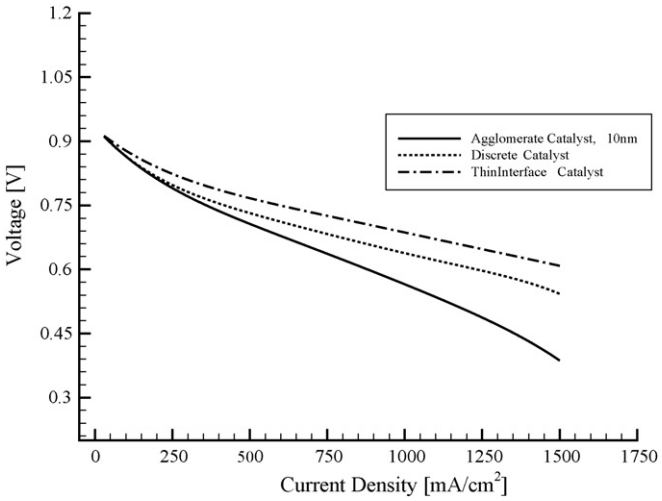

Fig. 9. Cathode polarization curve for the three catalyst models, $\delta = 10$ nm.

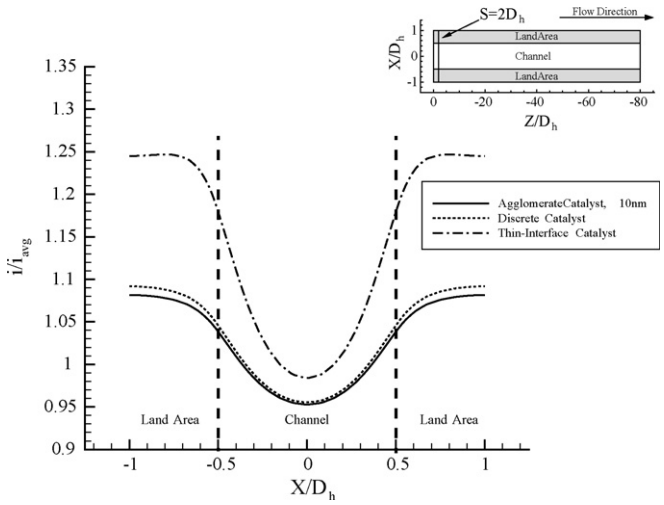

Fig. 10. Current density distribution near the inlet for the three catalyst models ($i = 100\,\mathrm{mA\,cm^{-2}}$).

varied such that the curves matched at very low currents and was then held constant for the remainder of the polarization curve. This method of altering the kinetics is common when comparing model data to experimentally measured polarization curves for poorly characterized electrodes (i.e. Ref. [9]); but is unnecessary when using the catalyst agglomerate model.

It is not surprising that the thin-interface model predicts the highest potential over the entire polarization curve, as it does not account for ohmic losses in the catalyst layer (ionic or electronic), nor does it account for the effect of the reduced porosity on mass transfer in the catalyst layer. The discrete-volume catalyst model does account for these effects, but it does not account for oxygen dissolution in the electrolyte phase, nor does it account for the effectiveness of catalyst utilization that occurs within an agglomerate structure. As such, the predicted polarization curve for the discrete model closely follows that of the agglomerate model up to a current density of approximately 200 $\mathrm{mA\,cm^{-2}}$. It then exhibits a very similar slope to the thin-interface model until a current density of about $1400\,\mathrm{mA\,cm^{-2}}$ where it begins to capture some mass transport losses.

Since both of the differences between the discrete-volume catalyst model and the catalyst agglomerate model are related to mass transport, it should be clear from this figure that mass transport effects due to the electrolyte film are evident in the polarization curve at current densities as low as $250\,\mathrm{mA\,cm^{-2}}$ (which is well before the visible inflection point) even with the use of a minimal electrolyte film thickness of 10 nm.

Figs. 10 and 11 compare the predicted current distributions near the inlet and near the outlet of the fuel cell, respectively, for each of the three catalyst models at a load of 100 $\mathrm{mA\ cm^{-2}}$. The curves are all normalized by $i_{avg} = 100\,\mathrm{mA\,cm^{-2}}$. As expected, the discrete-volume catalyst model and the catalyst agglomerate model predictions are very similar. The thin-interface model is quite different however, predicting significantly higher currents near the inlet, and significantly lower currents near the outlet. This behaviour stems from the fact that the kinetics of the reaction are artificially enhanced through the scaling of the effective catalyst area to account for the physical morphology of the catalyst which is not represented at all in the thin-interface approach. The resulting increased consumption of oxygen closer to the inlet yields reduced kinetics near the outlet due to lower oxygen concentrations. The net effect is that not only is the potential overpredicted, but current gradients are grossly over-predicted spatially along the cell using the thin-interface model. The difference between the maximum and minimum predicted current is $0.48 i_{avg}$ while it is approximately $0.21 i_{avg}$ for the other two models.

Fig. 12 compares the current density predictions of the three models near the fuel cell outlet for the highest load case of $i_{avg} = 1500\ \mathrm{mA\,cm^{-2}}$. For this load point, the thin-interface model and the discrete-volume model predictions are similar, with the thin-interface prediction consistently lower for the reasons described previously. The catalyst agglomerate model on the other hand is significantly different and is clearly showing evidence of mass transport limitations, consistent with the physics of the approach.

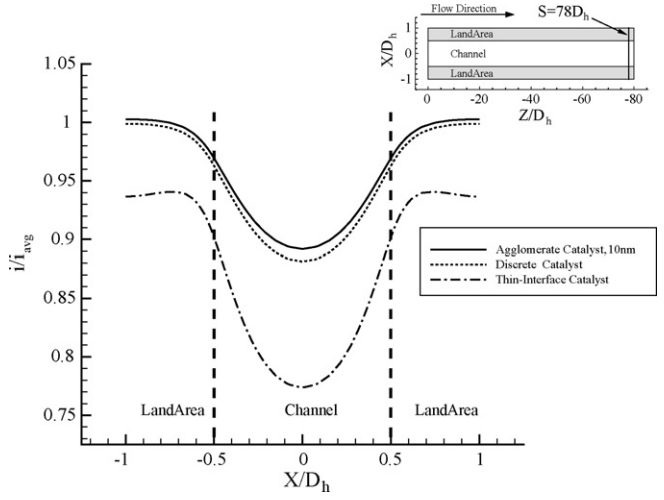

Fig. 11. Current density distribution near the outlet for the three catalyst models ($i = 100\,\mathrm{mA\,cm^{-2}}$).

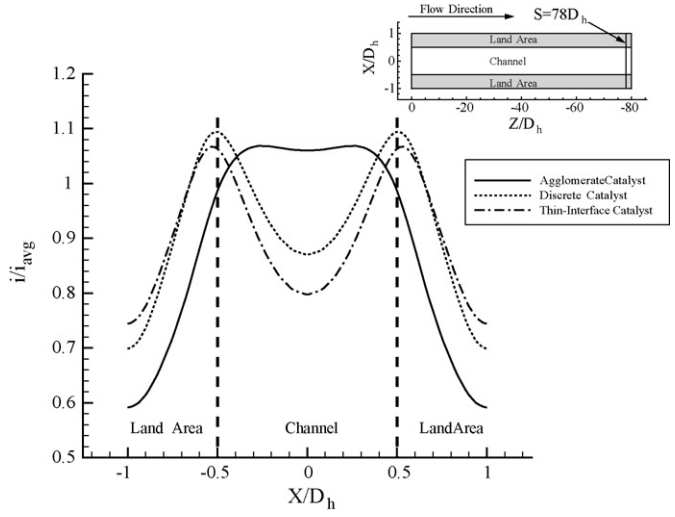

Fig. 12. Current density distribution near the outlet for the three catalyst models ($i = 1500\,\mathrm{mA\,cm^{-2}}$).

5. Conclusions

A three-dimensional implementation of a catalyst agglomerate model is described, and applied to a fuel cell with straight flow fields. The detailed results of this model are compared to the more commonly used thin-interface and discrete-volume catalyst models. It was found that the catalyst agglomerate model is capable of capturing all of the regions of the polarization curve—including the sharp drop off in performance at high currents. The results show that the thin-interface model significantly over-predicts the current gradients across the fuel cell in comparison to the two other approaches. Parametrically, the catalyst agglomerate model also shows the tendency for the results to be quite sensitive to the single remaining 'free parameter', the thickness of the electrolyte film which surrounds the agglomerates. This elicits the need for strong experimental characterization of the film thickness, particularly if accurate estimations of the mass transport related losses or limiting currents are desired.

Finally, even though relatively high stoichiometric ratios were used, clear evidence of mass transport 'limitations' are identified at very low currents, suggesting that it is a significant oversimplification to conceptualize the polarization curve using three distinct regions: activation, ohmic, and mass transport. This result also suggests that the observed experimental mass transport limitations of electrodes may not be solely attributable to liquid water, but that the electrode structure and morphology may also play as significant a role.

References

[1] W. Sun, B.A. Peppley, K. Karan, Electrochem. Acta 50 (16–17) (2005) 3359–3374.
[2] N.P. Siegel, M.W. Ellis, D.J. Nelson, M.R. von Spakovsky, J. Power Sources 115 (1) (2003) 81–89.
[3] M. Bang, S. Yde-Andersen, T.J. Condra, N. Djilali, E. Skou, Proceedings of the Conference on Hydrogen and Fuel Cells, 2003.
[4] S. Um, C.Y. Wang, J. Power Sources 125 (2004) 40–51.
[5] T. Zhou, H. Liu, J. Power Sources 125 (2004) 101–110.
[6] M. Bang, M. Odgaard, T.J. Condra, S.K. Kaer, Proceedings of the Second International Conference on Fuel Cell Science, Engineering and Technology, 2004.
[7] T. Berning, N. Djilali, J. Electrochem. Soc. 150 (12) (2003) A1589–A1598.
[8] P.W. Li, L. Schaefer, Q.M. Wang, T. Zhang, M.K. Chyu, J. Power Sources 115 (2003) 90–100.
[9] B.R. Siverstsen, N. Djilali, J. Power Sources 141 (2005) 65–78.
[10] C. Marr, X. Li, J. Power Sources 77 (1999) 17–27.
[11] J.G. Pharaoh, W. Sun, K. Karan, J. Power Sources 161 (1) (2006) 214–224.
[12] J.G. Pharoah, J. Power Sources 144 (2005) 77–82.
[13] D.B.P. Harvey, Master's Thesis, Queen's University at Kingston, Fuel Cell Research Centre, 2006.
[14] V. Minkmas, H. Williams, R. Kunz, J.M. Fenton, J. Electrochem. Soc. 151 (10) (2004) A1617–A1627.
[15] F.M. White, Viscous Fluid Flow, 2nd edition, McGraw-Hill, New York, NY, USA, 1991.
[16] Fluent Incorporated, Fluent 6.1 Documentation, 2003.
[17] R. Taylor, R. Krishna, Multicomponent Mass Transfer, 1st edition, John Wiley and Sons Inc., New York, USA, 1993.
[18] E.L. Cussler, Diffusion: Mass Transfer in Fluid Systems, 2nd edition, Cambridge University Press, Cambridge, United Kingdom, 1997.
[19] D.A. Nield, A. Bejan, Convection in Porous Media, 2nd edition, Springer-Verlag, New York, USA, 1998.
[20] T. Berning, PhD Thesis, University of Victoria, 2002.
[21] S.A. Boctor, et al., Electrical Concepts and Applications, West Publishing Company, Minneapolis, MN, USA, 1997.
[22] P. Berg, K. Promislow, J.St. Pierre, J. Stumper, B. Wetton, J. Electrochem. Soc. 151 (3) (2004) A341–A353.
[23] Z.H. Wang, C.Y. Wang, K.S. Chen, J. Power Sources 94 (2001) 40–50.
[24] L. You, H. Liu, Int. J. Heat Mass Transfer 45 (2002) 2277–2287.
[25] G.J.M. Janssen, M.L.J. Overvelde, J. Power Sources 101 (2001) 117–125.
[26] Y. Wang, C.-Y. Wang, J. Electrochem. Soc. 152 (2) (2005) A445–A453.
[27] J.H. Nam, M. Kaviany, Int. J. Heat Mass Transfer 46 (2003) 4595–4611.
[28] H. Meng, C.-Y. Wang, Chem. Eng. Sci. 59 (2004) 3331–3343.
[29] S. Dutta, S. Shimpalee, J.W. Van Zee, Int. J. Heat Mass Transfer 44 (2001) 2029–2042.
[30] K.-H. Choi, D.-H. Peck, C.S. Kim, D.-R. Shin, T.-H. Lee, J. Power Sources 86 (2000) 197–201.
[31] T.E. Springer, T.A. Zawodsinski, S. Gottesfield, J. Electrochem. Soc. 138 (8) (1991) 2334–2342.
[32] J.T. Hinatsu, M. Mizuhata, H. Takenaka, J. Electrochem. Soc. 141 (6) (1994) 1493–1498.
[33] M.J. Moran, H.N. Shapiro, Fundamentals of Engineering Thermodynamics, 4th edition, John Wiley and Sons Inc., New York, USA, 1999.
[34] J. Larminie, A. Dicks, Fuel Cell Systems Explained, 2nd edition, John Wiley and Sons Inc., Chichester, West Sussex, England, 2003.
[35] A.J. Bard, L.R. Faulkner, Electrochemical Methods—Fundamentals and Applications, 2nd edition, John Wiley and Sons Inc., New York, USA, 2001.
[36] W. Sun, B.A. Peppley, K. Karan, J. Power Sources 144 (2005) 42–53.
[37] A. Parthasarathy, S. Srinivasan, A.J. Appleby, C.R. Martin, J. Electrochem. Soc. 139 (10) (1992) 2856–2862.
[38] A. Parthasarathy, S. Srinivasan, A.J. Appleby, C.R. Martin, J. Electrochem. Soc. 139 (9) (1992) 2530–2537.
[39] T. Berning, D.M. Lu, N. Djilali, J. Power Sources 106 (2002) 284–294.
[40] D. Kramer, J. Zhang, R. Shimoi, Y. Ono, E. Lehmann, A. Wokaun, K. Shinohara, G.G. Scherer, Electrochim. Acta 50 (13) (2005) 2603–2614.
[41] G. Li, P.G. Pickup, J. Electrochem. Soc. 150 (11) (2003) C745–C752.
[42] A.A. Kulikovsky, J. Appl. Electrochem. 30 (9) (2000) 1005–1014.